# Effective Corrosion-Resistant Single-Atom Alloy Catalyst on HfO$_2$-Passivated BiVO$_4$ Photoanode for Durable (≈800 h) Solar Water Oxidation

*Maheswari Arunachalam, Kug-Seung Lee,\* Kai Zhu,\* and Soon Hyung Kang\**

Green hydrogen (H$_2$) production from solar water splitting necessitates photoelectrodes with superior photoelectrochemical (PEC) activity and durability. However, surface defects and photocorrosion instability—especially at high potentials—limit PEC performance and stability. Herein, the prototypical bismuth vanadate (BiVO$_4$) photoanode is used to demonstrate a holistic approach to improve photocurrent density and long-term stability. In this approach, high surface-area nanostructuring of BiVO$_4$ is combined with barium (Ba) doping with semi-crystalline hafnium oxide (HfO$_2$) surface passivation and single-atom nickel platinum (NiPt) catalysts. The introduction of Ba$^{2+}$ ions into BiVO$_4$ increases the concentration of conductive V$^{4+}$ ions or the ratio of V$^{4+}$ ions to oxygen vacancies, avoiding V$^{5+}$ dissolution during water oxidation. The semi-crystalline HfO$_2$, which serves as a passivation layer, prevents BiVO$_4$ photocorrosion by suppressing harmful chemical reactions when holes are transferred to the electrolyte. The synergistic use of isolated single-atom and Ni-Pt coordination improves charge transfer at the photoanode/electrolyte interface, leading to enhanced PEC kinetics and stability. As a result, a photoelectrode is demonstrated with ≈6.5 mA cm$^{-2}$ at 1.23 V versus a reversible hydrogen electrode (RHE) and continuous operation for 800 h with a negligible degradation rate. This work provides a promising approach to improve photoanodes for PEC H$_2$ production.

## 1. Introduction

Storing solar energy in hydrogen bonds via a photoelectro-chemical (PEC) process can contribute to achieving zero carbon emissions.[1,2] However, the PEC-based water splitting is limited by multiple factors, including light harvesting, recombination loss, and water oxidation kinetics.[3,4] PEC photoelectrode development requires a holistic approach to overcome these challenges. Monoclinic BiVO$_4$ is an interesting prototypical electrode material that can absorb a substantial part of the visible solar spectrum.[5] However, its poor charge transport can cause severe bulk and surface charge recombination loss—particularly at a low bias—at defects along the transport pathway. The reported charge separation efficiencies at potentials ≤0.6 V$_{RHE}$ remain lower than 70%.[6–10]

Charge transport properties and photocarriers separation in BiVO$_4$ can be improved with V site doping, increasing oxygen vacancies, and morphology tuning. Theoretical calculations also indicate the importance of doping sites for adsorption of hydroxyl (OH), oxygen (O), and hydroperoxyl (OOH) species on the electrode surface. The impurity doping can: 1) extend the optical absorption in the long wavelength range; 2) improve surface adsorption of chemical species; 3) enhance the electrical conductivity via modified charge carrier mobility, diffusion, or concentration; and 4) efficiently separate photogenerated charge carriers through a built-in electrical field near the solid–liquid interface.[11,12]

As the performance of BiVO$_4$-based photoanodes has continued to improve, the photostability of BiVO$_4$ has become an

M. Arunachalam, S. H. Kang
Department of Chemistry Education and Optoelectronic Convergence Research Center
Chonnam National University
Gwangju 61186, Republic of Korea
E-mail: skang@jnu.ac.kr

K.-S. Lee
Pohang Accelerator Laboratory
Pohang University of Science and Technology (POSTECH)
Pohang 37673, Republic of Korea
E-mail: lks3006@postech.ac.kr

K. Zhu
Chemistry and Nanoscience Center
National Renewable Energy Laboratory
Golden, CO 80401, USA
E-mail: Kai.Zhu@nrel.gov

The ORCID identification number(s) for the author(s) of this article can be found under https://doi.org/10.1002/aenm.202402607

**ADVANCED
SCIENCE NEWS**

www.advancedsciencenews.com

**ADVANCED
ENERGY
MATERIALS**

www.advenergymat.de

important issue. The harmful photocorrosion involving selective leaching of vanadium (V) still prevents the continuous application of $BiVO_4$.[13,14] Hence, it is valuable to design an effective corrosion-resistant layer to mitigate the dissolution of the underlying components without hindering charge transfer and photon absorption. For example, a W-doped $BiVO_4$ photoanode passivated with a thin amorphous $TiO_x$ layer by electrodeposition can suppress the back reduction of photo-oxidized products.[15] In another study, an ultrathin $Al_2O_3$ coating was deposited on $BiVO_4$ electrodes to passivate the surface states using an atomic layer deposition (ALD)-like process.[16] For the $TiO_x$-passivated $BiVO_4$ photoanode, although the performance is improved, the photocurrent density is still lower than 0.25 mA cm$^{-2}$, which is presumably limited by charge transfer. Notably, the $TiO_x$ layer contains positive charges, producing local electric fields at the interface. Consequently, photocarriers (electrons and holes) will migrate to the electrolyte and substrate sides, resulting in a decrease in the photocurrent density of the photoelectrode. Thus, the selection of passivation material is crucial, as it can affect both the PEC performance and stability.

The use of a catalyst layer can also suppress photocorrosion by increasing the rate of interfacial charge transfer. However, the stability of the catalyst could become an issue when the photoelectrode is operating at a high photocurrent density coupled with a high operational potential. Recently, the $Sn/Ni/Mo:BiVO_4/NiFeO_x$ photoanode exhibited enhanced photocorrosion inhibition and self-generation and regeneration of oxygen evolution catalysts, leading to stable oxygen evolution for >1000 h at low potentials (as low as 0.4 V$_{RHE}$).[17] Another study revealed that the presence of $V^{5+}$ species in the electrolyte can form a vanadium-containing surface layer on FeOOH/NiOOH, enhancing water-oxidation kinetics over 500 h; note that this phase was not stable under conventional water oxidation conditions due to vanadium loss.[18] The water oxidation capability of co-catalysts is limited by the insufficient thermodynamic driving force for hole extraction from the photoanodes.

The poor interaction at the photoanode–catalyst interfaces could induce high electrical resistance or produce recombination centers, limiting the hole transport to the oxygen evolution reaction (OER) catalysts. This hole transport is critical for participating in water oxidation reactions. A recent study reported that Pt-based catalysts are unstable under high anodic potentials, potentially dissolving into electrolytes because of conversion to high oxidation states.[19] In contrast, single-atom catalysts (SACs) have smaller dimensions and higher surface-to-volume ratios, which favor lowering the catalyst cost and enhancing the catalytic performance. Although it is desirable to use SACs with a controlled charge distribution and coordination environment to improve the photoanode's OER performance, pushing catalysts to the single-atom scale is nontrivial as SACs tend to aggregate into clusters or nanoparticles.[20,21]

In this study, we report on a holistic approach—encompassing nanostructuring, doping, surface passivation, and SAC—to significantly enhance the performance and operational stability of the $BiVO_4$ photoanode. We first report a unique nano-leaf-like-structured Ba-doped $BiVO_4$ (referred to as Ba:$BiVO_4$) electrodeposited on the Fluorine-doped tin oxide (FTO) conducting substrate. Before the Ba:$BiVO_4$ deposition, a 10-nm interlayer of ALD $SnO_2$ was coated to facilitate electron transfer from $BiVO_4$ to

FTO by reducing the back recombination. Next, we introduced ALD-coated semi-crystalline hafnium oxide ($HfO_2$) as a protection layer with several preferred features: 1) it is stable over a wide range of pH and potential values; 2) it acts as a barrier to mitigate physical and chemical degradation; and 3) it does not hinder charge transport to the electrode. The $HfO_2$ layer helps maintain efficient electrode operation while mitigating degradation pathways. Particularly, the semi-crystalline passivation layer exhibits enhanced charge transfer efficiency due to the synergistic interplay of amorphous regions (high density of localized states) and crystalline regions (inherent structural order). We further combined the nanostructured Ba:$BiVO_4$/$HfO_2$ photoanode support with a single-atom alloy, NiPt co-catalyst, synthesized by electrochemical deposition. The co-catalyst exhibits atomically dispersed Pt atoms, stabilized on the surface of Ni nanoclusters through Pt-Ni coordination accompanied with electron transfer from Ni to Pt. With such a holistic development approach, we achieved unprecedented photocurrent densities of up to 6.2 mA cm$^{-2}$ under simulated AM 1.5G illumination and ≈800-h operation with a negligible degradation rate for water oxidation at 1.23 V$_{RHE}$. The NiPt SAC is atomically well dispersed on the Ba:$BiVO_4$/$HfO_2$ photoanode. It not only provides an effective OER catalytic function but also increases the optical absorption and hole lifetime of the photoanode. Our study demonstrates an effective approach for integrating photoanodes with surface passivation and single-atom co-catalyst support to enable efficient photoelectrode operation, which is attractive for large-scale PEC cell development.

## 2. Results and Discussion

### 2.1. Chemical and Physical Properties of the Ba:$BiVO_4$/$HfO_2$/NiPt Photoanode

**Figure 1a** illustrates the systematic synthesis process for preparing the Ba:$BiVO_4$/$HfO_2$/NiPt photoanode. Scanning electron microscopy (SEM) shows that $BiVO_4$ has a leaf-like nanostructure with multi-leaves composed of very small crystallites. This larger-surface-area photoanode can interact with a larger volume of electrolyte and thus facilitate more water oxidation reactions. This means that the massive holes can be used to oxidize water into oxygen and protons, instead of recombining with the electrons. When light hits a nanostructured surface, it can get trapped within the material and bounce around, leading to multiple interactions with the material and an increased probability of absorption. Top-view SEM images (Figure 1c) show that the Ba dopant did not change the surface morphology. The $HfO_2$-covered Ba:$BiVO_4$ shows a smooth morphology, indicating that the coverage of the passivation layer deposited via ALD is uniform (Figure 1d).

Furthermore, the NiPt alloy (Figure 1e), in the form of tiny spherical particles arranged on the entire surface of the Ba:$BiVO_4$/$HfO_2$ photoanode, suggests that electrodeposition of the NiPt catalyst forms well-bounded interfaces within the passivated photoanode. After the coating of the NiPt catalysts, the smooth surfaces of the Ba:$BiVO_4$/$HfO_2$ photoanodes transformed into a slightly rough texture. Low-magnification SEM (Figure S1, Supporting Information) revealed a well-defined, high-surface-area nanostructured $BiVO_4$ on the conducting
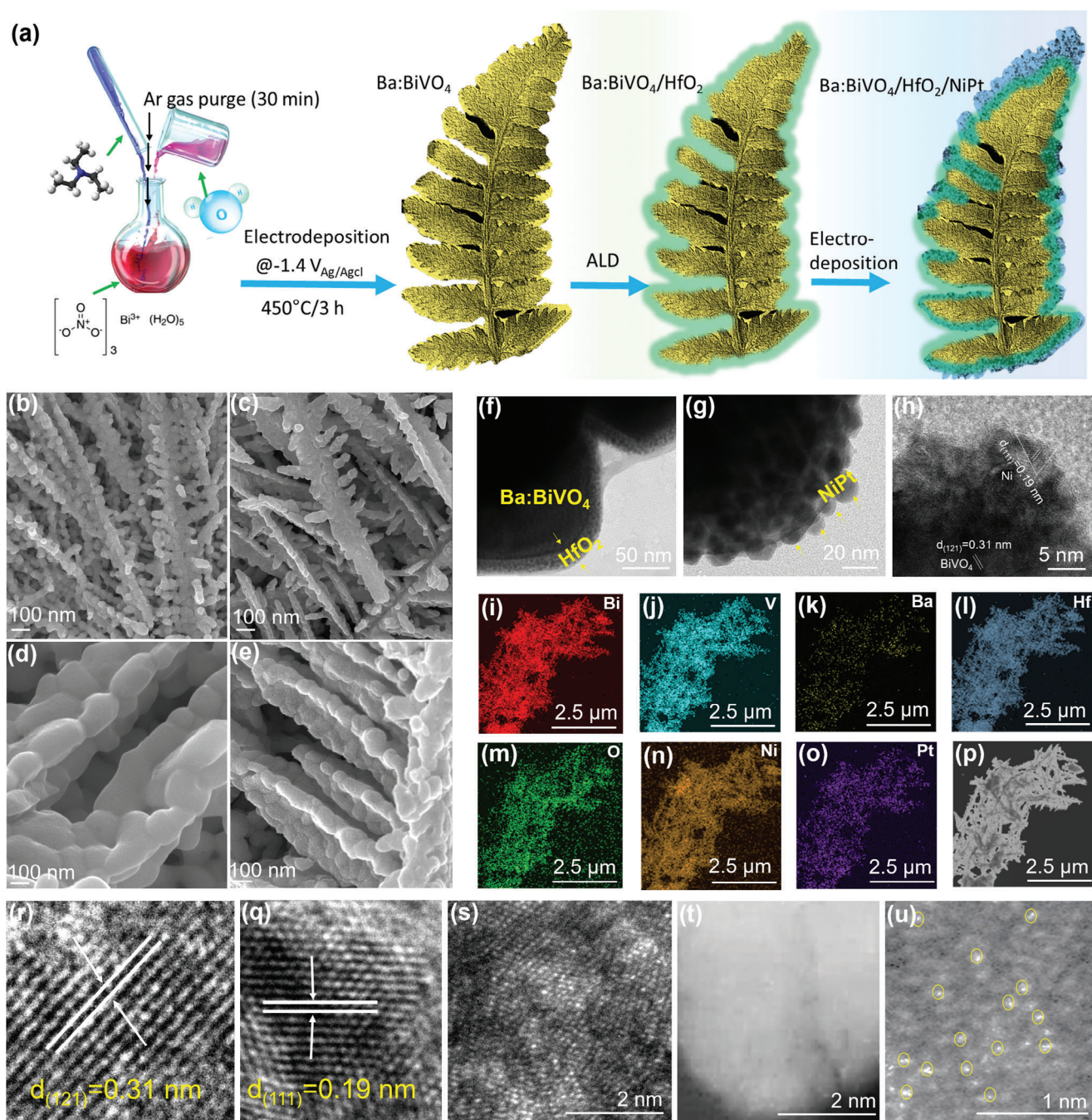
**ADVANCED**
SCIENCE NEWS

www.advancedsciencenews.com

**ADVANCED
ENERGY
MATERIALS**

www.advenergymat.de

**Figure 1.** a) Schematic illustration of photoanode fabrication process. b–e) Field-emission Scanning electron microscopy (FE-SEM) images of $BiVO_4$, $Ba:BiVO_4$, $Ba:BiVO_4/HfO_2$, and $Ba:BiVO_4/HfO_2/NiPt$. f–h) HR-TEM images of $Ba:BiVO_4/HfO_2$ and $Ba:BiVO_4/HfO_2/NiPt$. i–p) EDS mapping of each element such as Bi, V, Ba, Hf, O, Ni, and Pt, respectively. HR-TEM image of $Ba:BiVO_4/HfO_2/NiPt$ photoanode film indicating clear lattice lines corresponding to (r) $BiVO_4$ and q) Ni. s–u) High-angle annular dark-field Cs-STEM images of NiPt deposited $Ba:BiVO_4/HfO_2$ photoanode film with the isolated Pt atom highlighted in a yellow circle.

substrate, fabricated using an optimized synthesis protocol. We conducted high-resolution transmission electron microscopy (HR-TEM) to further explore the surface morphology and structure (Figure 1f–h). Figure 1f shows the $Ba:BiVO_4/HfO_2$ photoanodes has a thin (≈10 nm) passivation layer, confirming the formation of $HfO_2$ on the surfaces of the $Ba:BiVO_4$ photoanode.

Figure 1g illustrates the NiPt-covered $Ba:BiVO_4/HfO_2$ photoanode with a detailed interface between the passivation layer and the surrounding NiPt co-catalyst. As displayed in Figure 1h, a number of bright spots are clearly observed, further confirming the formation of single metal-atom pairs. Notably, spherical aberration (Cs) -corrected transmission electron microscopy

(HAADF-STEM) images (Figure 1i,j) clearly show that single-atom alloy NiPt catalysts are uniformly dispersed on the surface of the Ba:BiVO$_4$/HfO$_2$ photoanode, without cluster or aggregation. Furthermore, the Pt atoms were confirmed by the isolated single atom in the STEM image (Figure S2, Supporting Information), revealing the ordered intermetallic NiPt alloy with high crystallinity. According to Figure 1i, the lattice lines of the (121) plane with an interspacing of 0.31 nm correspond to highly crystallized BiVO$_4$ in the bulk region, and the fringes on the top side with interplanar distance of 0.19 nm correspond to the Ni (111) plane, respectively. Moreover, the energy dispersive spectroscopy (EDS) elemental mapping images are shown in Figure 1i–p. In these images, signals of Bi, V, Ba, O, Ni, and Pt elements could be detected, suggesting the homogeneous distribution of the HfO$_2$ and NiPt catalysts on the Ba:BiVO$_4$ photoanode with the quantitative wt.% content of constituent elements Bi (58.00%), V(14.00%), O(15.00%), Ba(2.50%), Hf(1.18%), Pt(3.20%), and Ni(6.12%). Figure 1q,r shows the interplanar distances of BiVO$_4$ and Ni as depicted in Figure 1h. Figure 1s–u presents HAADF–STEM images that provide a detailed view of the isolated atoms in the electrocatalyst. In these images, the bright spots representing Pt single atoms are marked with yellow circles.

**Figure 2** shows the X-ray diffraction (XRD) patterns of pristine BiVO$_4$, Ba:BiVO$_4$/HfO$_2$, and Ba:BiVO$_4$/HfO$_2$/NiPt samples; all of the high-intensity diffraction peaks are consistent with the monoclinic phase of BiVO$_4$ (Joint Committee on Powder Diffraction Standards number (JCPDS) #14-0688). The XRD peaks of the monoclinic BiVO$_4$ shift to lower angles in Ba:BiVO$_4$ film, due to the dissimilarity between the ionic radius of the host lattice and dopant ion; this suggests that dopant ions are incorporated interstitially in the BiVO$_4$ lattice f BiVO$_4$. Because of the phase purity and modification in $d$ spacing, it can be concluded that Ba impurities have been successfully incorporated into the crystal lattice of BiVO$_4$ as interstitial dopants, while the monoclinic phase structure is preserved. The XRD spectra in Figure S3 (Supporting Information) clearly highlight the shift to lower angles observed in the Ba:BiVO$_4$ film.

It was not found that the developed films have sub-oxide impurities such as BiO$_X$ and VO$_X$ phases. However, the low-intensity diffraction peaks corresponding to HfO$_2$ (JCPDS # 006–0318) were observed at 34.6° from the (002) plane. This is attributed to the semi-crystalline monoclinic structure and ultrathin ($\approx$10 nm) nature of the HfO$_2$ film. The HfO$_2$ peak intensity was notably weaker compared to that of BiVO$_4$. Crystalline cubic NiPt alloys at 51.5° assigned to the main (111) crystal plane of Ni were successfully prepared on a Ba:BiVO$_4$/HfO$_2$ and the absence of XRD peaks for metallic Pt precludes the possibility of single-atom dispersion of Pt.

For more clear evidence, we utilize other techniques sensitive to electronic interactions, such as X-ray absorption spectroscopy (XAS) to provide further evidence on the Pt-Ni interaction (Figure 2b–e). The X-ray absorption near-edge structure (XANES) spectra of Ni K-edge for NiPt showed a significant positive shift compared to the Ni-foil reference and synthesized Ni sample, suggesting the presence of oxidized Ni species in NiPt (Figure 2b). Prominent peaks in the Fourier transformed extended X-ray absorption fine structure (FT-EXAFS) spectra at $\approx$2.1 Å for Ni foil and Ni sample identified the Ni—Ni bond in Ni

fcc metallic phase (Figure 2d). Notably, the Ni—O bond located at 1.6 Å indicated that Ni was oxidized to form an oxide phase as mentioned in the XANES analysis.[22]

The Pt L$_3$-edge XANES spectra (Figure 2c), reveal that the rising edge of the NiPt single-atom catalyst slightly shifted to higher energies, implying that the Pt element in NiPt sample was minutely oxidized from its metallic phase. The minute oxidation of Pt might be attributed to Pt—C and/or Pt—O bondings formed during the synthesis since the NiPt sample was synthesized process. Further insights are provided by the FT-EXAFS spectra of Pt (Figure 2e), which confirms the metallic state of both Pt and Pt foil, as indicated by the Pt—Pt bond at $\approx$2.5 Å. In the NiPt sample, a shift of this peak to lower energy suggests the presence of a Pt—Ni bond. Additionally, the potential Pt—C and/or Pt—O bonds as stated in the XANES analysis might be obscured in the region between 1.5 and 2.0 Å.[23,24]

We further explored the chemical states and electronic structures of the Ba:BiVO$_4$/HfO$_2$/NiPt photoanodes via high-resolution X-ray photoelectron spectroscopy (XPS). Figure 2b shows the typical characteristics of Bi$^{3+}$ species on the BiVO$_4$ electrode, as evidenced by the peaks of Bi4$f_{5/2}$ and Bi4$f_{7/2}$ at binding energies (BEs) of 164.61 and 159.07 eV, respectively. Figure 2c shows the V2$p_{1/2}$ and V2$p_{3/2}$ peaks of BiVO$_4$ located at BEs of 524.10 and 516.92 eV, respectively, indicating the formation of V$^{5+}$ cations in the crystal lattice.[25–27] In the Bi4$f$ spectra, we observed an obvious shoulder peak at a high BE of 160.3 eV, attributable to the high-valence Bi$^{(3+x)}$ species; in the V2$p$ spectra, we observed a shoulder peak at 515.5 eV, which can be assigned to the low-valence V$^{(5-x)}$ species.[28] This is possibly due to changes in their local coordination environments or partial chemical reduction in the presence of oxygen vacancies and Ba$^{2+}$ substitution on the BiVO$_4$ lattice, which may increase the electron density of the V and Bi atoms. The presence of oxygen vacancies was further confirmed by electron paramagnetic resonance (EPR) spectroscopy and Raman spectra (Figure S5a,b, Supporting Information).[29–31] For core-level Ba3$d$ XPS spectra (Figure 2d), we found two deconvoluted peaks associated with Ba3$d_{7/2}$ at 780.7 eV and Ba3$d_{5/2}$ at 795.5 eV, ascribed to the oxidation state of Ba$^{2+}$. The atomic concentrations of Ba obtained from XPS survey spectra were 3 wt.% for the Ba:BiVO$_4$. To gain further insight into the effect of Ba doping, we also analyzed the O1$s$ and V2$p$ spectra. The doping of Ba$^{2+}$ ions into the BiVO$_4$ lattice causes abundant V$^{4+}$ species and oxygen defects, leading to shortened charge transport length and enhanced optical absorption.

Furthermore, the O1$s$ spectrum can be fitted into three peaks located $\approx$529.55, 531.66, and 532 eV, which can be assigned to O$^{2-}$ species in the lattice (O$_L$), hydroxyl groups bonded to the metal cations in the oxygen-deficient region (O$_V$), and chemisorbed or dissociated oxygen species such as adsorbed H$_2$O or adsorbed O$_2$, respectively.[28] In Figure 2e, the Hf4$f$ exhibited the +4 oxidation state related to Hf4$f_{7/2}$ and Hf4$f_{5/2}$, positioned at BEs of 18.1 and 21.4 eV, and the metallic and sub-oxide hafnium were also positioned at BEs of 15.1 and 16.2 eV, respectively. According to these findings, some mixed semi-crystalline oxide structures form in the crystalline HfO$_2$, and these are responsible for driving the significant oxidation of the PEC water.[32]
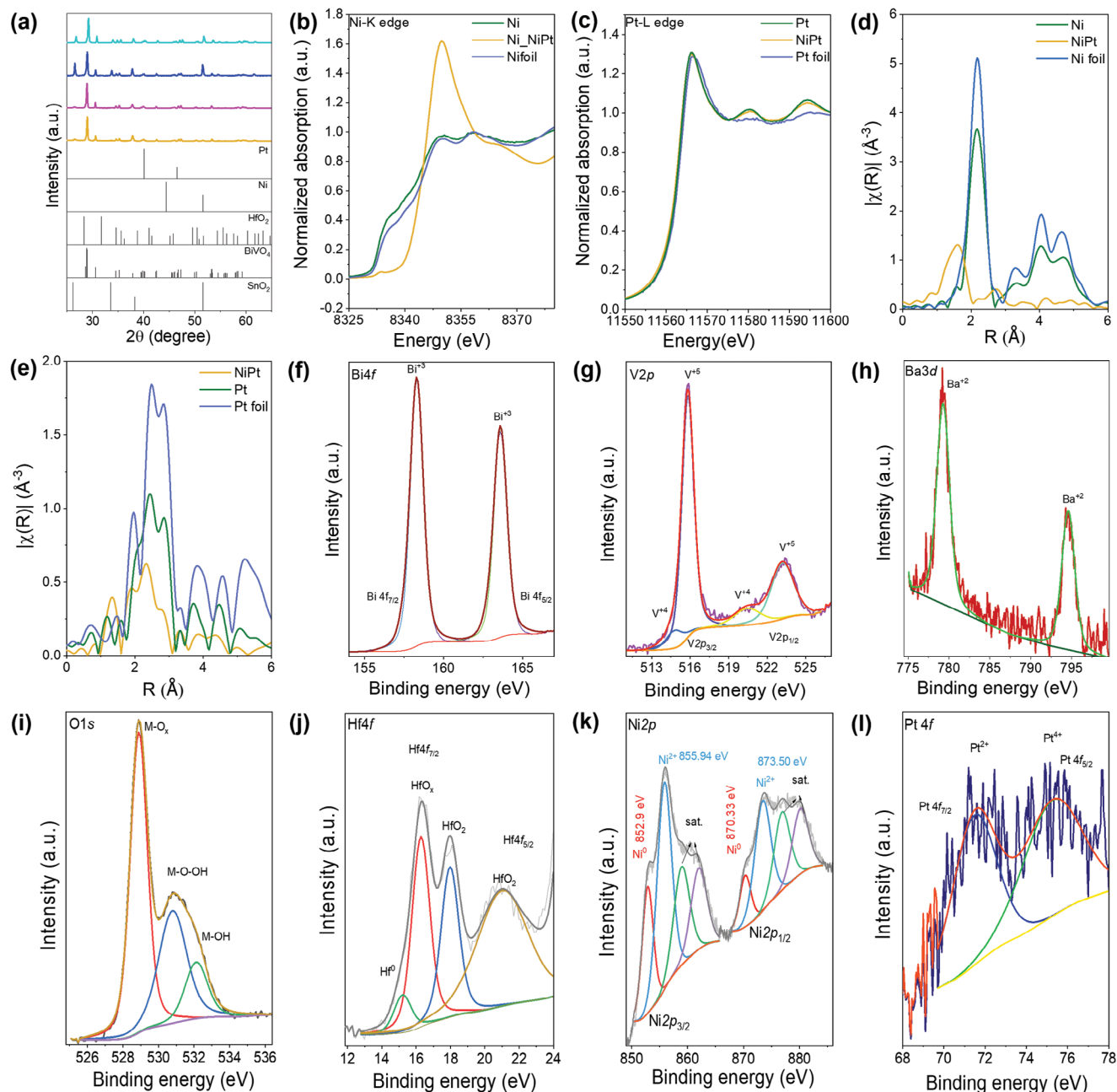
**Figure 2.** a) XRD of BiVO₄ (yellow), Ba:BiVO₄ (magenta), Ba:BiVO₄/HfO₂ (blue), and Ba:BiVO₄/HfO₂/NiPt (cyan) photoanode films. b) Ni K-edge XANES spectra of Ni-foil, Ni, and NiPt, c) Pt L-edge XANES spectra of Pt-foil, Pt, and NiPt, d) FT–EXAFS spectra Ni-foil, Ni and NiPt, and e) FT–EXAFS spectra of Pt-foil, Pt and NiPt. High-resolution XPS spectra for f) Bi4$f$, g) V2$p$, h) Ba3$d$, i) O1$s$, j) Hf4$f$, k) Ni2$p$, and l) Pt4$f$ for Ba:BiVO₄/HfO₂/NiPt photoanodes.

For the Ni2$p$ characteristic peaks (Figure 2g), two peaks of Ni$^{\delta+}$ at 854.03 and 866.98 eV were assigned to the Ni2$p_{3/2}$ and Ni2$p_{1/2}$ levels, respectively. Each level was further split into two peaks at 855.55 and 873.08 eV, representing the coexistence of the Ni$^{2+}$ oxidation state. This suggests the existence of multiple Ni oxidation states are present in the alloyed NiPt phase. Nickel hydroxide can participate in reversible (Ni$^{2+}$ to Ni$^{\delta+}$) redox reactions, providing additional sites for the OER process. The other peaks at 861 and 880 eV were satellite peaks, consistent with

the Ni2$p$ spectra reported in previous studies. Figure 2h shows the Pt 4$f$ core-level spectra of NiPt. Pt4$f_{7/2}$ and Pt4$f_{5/2}$ orbitals of the NiPt are observed at BEs of 72.4 and 74.8 eV, respectively. This confirms the presence of Pt atoms with partially positive charge (Pt$^{\delta+}$4$f_{7/2}$ and Pt$^{\delta+}$4$f_{5/2}$) owing to the electronic interaction between single Pt atoms and Ni. This peak position can be regarded as evidence for the presence of surface Pt single atoms. More importantly, Pt SACs with strong electronegativity were deposited on the Ba:BiVO₄/HfO₂/NiPt, changing the electron cloud

**2402607 (5 of 12)**

**ADVANCED
SCIENCE NEWS**

www.advancedsciencenews.com
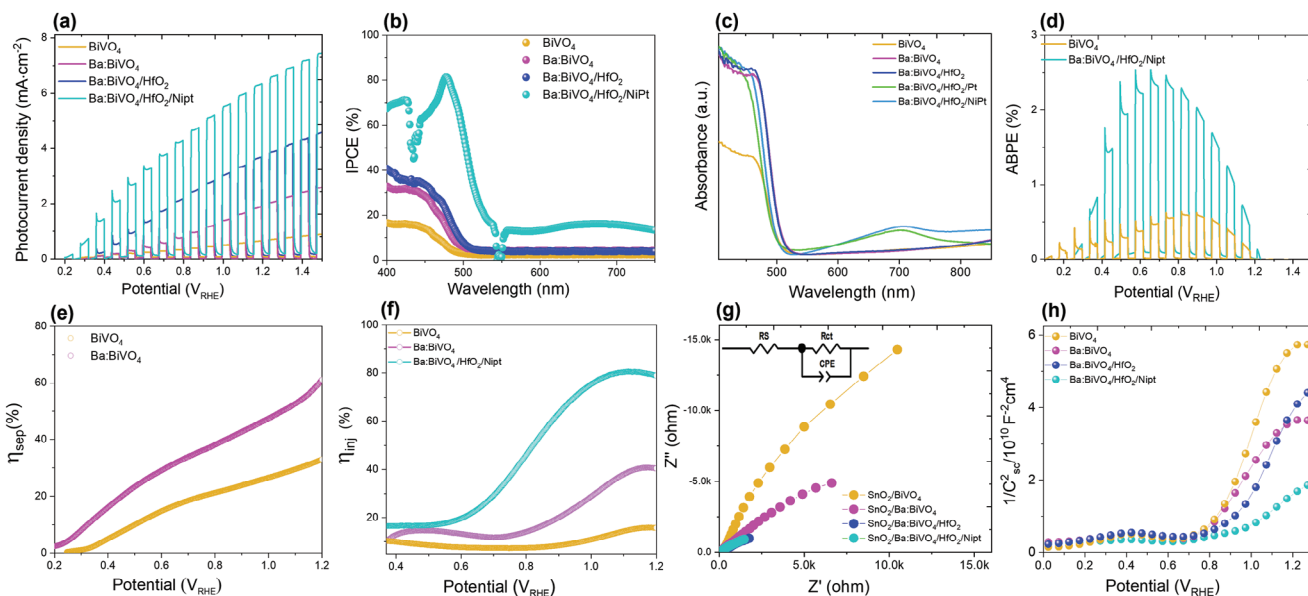
**ADVANCED
ENERGY
MATERIALS**

www.advenergymat.de

**Figure 3.** a) Chopped LSV curves, b) incident photon-to-current efficiency spectra (at 1.23 $V_{RHE}$), c) UV-vis diffusive absorbance spectra, d) ABPE, e,f) charge separation and injection efficiency, g) EIS Nyquist plots (at open-circuit potential), and h) Mott–Schottky plots (at 1 kHz under dark) of the photoanode films.

density.[28,33] The increased electron cloud density facilitates electron transfer from Ni to Pt via the Pt—O—M bond, which facilitates the transfer of holes from Ba:BiVO₄/HfO₂ to NiPt for OER. To further understand the crystalline properties and chemical composition, we directly deposited NiPt onto Ti foil substrate, as shown in Figure S4 (Supporting Information).

## 2.2. Photoelectrochemical Activity

PEC water splitting activities were evaluated in 1 M KBi electrolyte by a standard three-electrode system under AM 1.5G 1-sun illumination. As shown in **Figure 3a**, the highest photocurrent density $J_{ph}$ of ≈6.5 mA cm⁻² was achieved for Ba:BiVO₄/HfO₂/NiPt, followed by Ba:BiVO₄/HfO₂ ($J_{ph}$ ≈ 3.9 mA cm⁻²) and Ba:BiVO₄ ($J_{ph}$ ≈ 2.1 mA cm⁻²), whereas undoped BiVO₄ gave a $J_{ph}$ value of ≈0.77 mA cm⁻². The pristine BiVO₄ photoanode exhibited a relatively low $J_{ph}$ value, which is attributable to both a high surface defect density and slow charge transfer kinetics, causing recombination losses at the surface. The HfO₂ passivated photoanode exhibited an early onset (0.28 $V_{RHE}$) with a large current density. This is attributed to surface defect passivation by HfO₂, which can suppress charge recombination at the Ba:BiVO₄ surface for efficient charge transport. The surface charge transfer kinetics can be improved by applying the catalyst a top Ba:BiVO₄/HfO₂. The NiPt catalysts on top of BiVO₄ photoanodes promoted the water oxidation reaction, and an outstanding $J_{ph}$ together with a low onset potential ($V_{on}$) for the OER has been achieved. The atomically dispersed NiPt co-catalyst can eliminate the unnecessary charge recombination and the non-Faradaic charging process, leading to a significant cathodic shift in $V_{on}$ (≈0.195 $V_{RHE}$) and improved $J_{ph}$ in the entire potential range. This phenomenon is verified by the OER activity of the NiPt catalyst in 1 M KOH (Figure S6, Supporting Information). In addition, the effect of Pt

SAC on PEC performance, relative to SnO₂/Ba:BiVO₄/HfO₂/Ni photoanode, is shown in Figure S7 (Supporting Information).

We further conducted the incident photon-to-current conversion efficiencies (IPCEs) at 1.23 $V_{RHE}$, and the results are shown in Figure 3b. The IPCE at 480 nm reaches 7% for the BiVO₄ photoelectrode. The IPCE increases from 0% at ≈510 nm to 18% at ≈450 nm and remains almost constant until it starts to decrease at ≈400 nm. The decrease is due to the parasitic absorption by the FTO glass. After the decoration of the NiPt catalysts, the IPCE values of the BiVO₄ photoanodes are much enhanced in the whole absorption wavelength range, with the extension of photon harvesting up to 800 nm. Also, the enhancement within the 520–800 nm spectral region can be attributed to the scattering and reflection of incident light by dispersed NiPt particles embedded within the BiVO₄ layer, thereby elevating the probability of photon absorption and contributing to improved solar energy conversion. The enhanced solar conversion efficiency (≈83%) before 520 nm can be mainly attributed to the enhanced charge separation efficiency (≈80%).

We explored the optical properties of pristine BiVO₄, Ba:BiVO₄, Ba:BiVO₄/HfO₂, and Ba:BiVO₄/HfO₂/NiPt photoanodes using ultraviolet-visible (UV-vis) absorption spectra (Figure 3c). For the bare BiVO₄ film, the onset of light absorption is ≈514 nm, corresponding to its bandgap energy. In the Ba:BiVO₄, the band absorption edges shifted to longer wavelengths, including the improvement of the $E_g$ value. It is interesting to note that HfO₂ did not alter the optical properties of Ba:BiVO₄. Hence, the HfO₂ layer is thin enough to collect solar spectrum efficiently. The introduction of NiPt resulted in a redshift of the onset wavelength, extending the spectral response up to 800 nm. This can reflect the optimized interfacial interaction between atomically dispersed NiPt and the BiVO₄ photoanode, facilitating enhanced charge transfer and improved photon utilization. To clearly determine the

**Table 1.** Simulated values of each type of photoelectrodes using the suggested equivalent circuit model along with the corresponding flat-band potential and carrier concentration.

| Photoanodes | $R_S$ [Ω] | $R_{CT}$ [Ω] | $V_{FB}$ [vs. RHE] | $N_D$ [cm$^{-3}$] |
|---|---|---|---|---|
| BiVO$_4$ | 25 | 10 400 | 0.35 | 3.982*10$^{16}$ |
| Ba:BiVO$_4$ | 18 | 3376 | 0.28 | 4.757*10$^{16}$ |
| Ba:BiVO$_4$/HfO$_2$ | 22 | 750 | 0.23 | 1.363*10$^{17}$ |
| Ba:BiVO$_4$/HfO$_2$/NiPt | 20 | 405 | 0.187 | 3.875*10$^{18}$ |

potential-dependent solar conversion efficiency, we measured the applied bias photon-to-current efficiency (ABPE) (Figure 3d). The BiVO$_4$ and Ba:BiVO$_4$/HfO$_2$/NiPt achieved maximum ABPEs of 0.5% and 2.5%, respectively, at 0.8 $V_{RHE}$ with AM 1.5G 1-sun illumination.

To have a better understanding of the enhanced water oxidation performance of the photoanode, we investigated the charge carrier dynamics (i.e., charge injection and charge separation). We calculated the charge-injection and -separation efficiencies by performing linear sweep voltammetry (LSV) with a sulfite oxidation reaction in a 1 M KBi electrolyte containing 0.2 M of Na$_2$SO$_3$ (pH 9.0) under AM 1.5G illumination. The calculated charge separation ($\eta_{sep}$) and injection efficiency ($\eta_{inj}$) are presented in Figure 3e and f, respectively. The $\eta_{sep}$ and $\eta_{inj}$ values can be extracted from the following Equations (1 and 2):[34]

$$\eta_{sep} = J_{Na_2SO_3}/J_{abs} \tag{1}$$

$$\eta_{inj} = J_{H_2O}/J_{Na_2SO_3} \tag{2}$$

Figure 3e shows the $\eta_{sep}$ curves for the BiVO$_4$ and Ba:BiVO$_4$ photoanodes. For both electrodes, the separation yield begins to rise at the anodic part of the flat band potential, reaching 36% and 60% for the BiVO$_4$ and Ba:BiVO$_4$, respectively, at a potential of 1.23 $V_{RHE}$. The successful doping of the impurity into the BiVO$_4$ lattice implies an enhancement in the charge separation efficiency. Moreover, the $\eta_{inj}$ of both BiVO$_4$ and Ba:BiVO$_4$ were below 50% (Figure 3e), which suggest that more than half of the photogenerated holes were lost due to surface recombination. Notably, the Ba:BiVO$_4$/HfO$_2$/NiPt photoanode exhibited a significantly higher $\eta_{inj}$ of 80%, implying a rapid enhancement in injection yield at high anodic potentials, most likely resulting from surface trap passivation at the electrode/electrolyte interface. Apparently, NiPt led to nearly complete charge injection from the bulk BiVO$_4$ into the surface sites for the OER, avoiding charge recombination loss.

Figure 3g shows the results of the electrochemical impedance spectroscopy (EIS), which we used to further elucidate the interfacial charge transfer properties. We selected the Randles model, in which $R_S$ is the electrolyte resistance, CPE is the capacitance phase element for the semiconductor/electrolyte interface, and $R_{CT}$ is the charge transfer resistance across the interface. The best-fit results with the equivalent circuit model in Figure 3g were summarized in **Table 1**. The arcs in the Nyquist plot are related to charge transfer at the photoelectrode/electrolyte interface. According to the Nyquist plots and the fitting results, the calculated resistances are observed in the photoelectrodes (in order: Ba:BiVO$_4$/HfO$_2$/NiPt > Ba:BiVO$_4$/HfO$_2$ > Ba:BiVO$_4$ > BiVO$_4$)

under illumination. This reveals that the preferable capability of the interfacial resistance of the Ba:BiVO$_4$/HfO$_2$/NiPt films is much smaller than that of bare BiVO$_4$. This facilitates efficient charge transfer at the interface between the photoelectrode and electrolyte and in particular, the HfO$_2$ overlayer not only facilitates the transfer of photogenerated holes but also aids in the release of accumulated charges from the photoelectrode surface into the electrolyte, hindering the charge recombination and inducing the facile charge transport of electrons through the films. Overall, we attribute the enhanced PEC water oxidation performance of the Ba:BiVO$_4$/HfO$_2$/NiPt film to the improved transport of photocarriers across the thin HfO$_2$ passivation layer to eventually reaching the active sites of the NiPt electrocatalyst for the PEC water oxidation reaction.

To evaluate the flat-band potential and hole carrier density of the photoanode, we measured Mott–Schottky plots at 1 kHz in dark conditions (Figure 3h), including the values presented in Table 1. The flat band potential ($E_{FB}$) is negatively shifted, and the carrier (electron) density increases toward the Ba:BiVO$_4$/HfO$_2$/NiPt < Ba:BiVO$_4$/HfO$_2$ < Ba:BiVO$_4$ < BiVO$_4$ films. The Ba:BiVO$_4$ generates more donor states in the bandgap, and the increase in donor density influences the favorable charge separation and transfer event. The increase of charge carrier density by HfO$_2$ confirms fewer surface states and reduced recombination due to the passivation effect. To have a better understanding of the photogenerated carrier transfer kinetics and changes in the density of surface states of the Ba:BiVO$_4$/HfO$_2$/NiPt photoanode, we carefully performed EIS analyses as a function of applied potential (**Figure** 4a–e).

## 2.3. Interfacial Charge Transfer Process and Surface States (SS)

A larger value of trap capacitance ($C_{ss}$) and a lower value of charge transfer resistance would normally result in a larger photocurrent associated with a more effective charge transfer from SS.[35] Figure 4a shows the best fitted bulk charge transfer resistance ($R_{bulk}$) as a function of applied potentials. The Ba:BiVO$_4$/HfO$_2$/NiPt shows the smallest $R_{bulk}$ over the entire potential range, followed by bare Ba:BiVO$_4$/HfO$_2$, Ba:BiVO$_4$, and 6% BiVO$_4$. Upon doping of the Ba element into BiVO$_4$, we achieve a lower $R_{bulk}$, suggesting that the Ba doping employed herein improves the charge transfer in the bulk. Analysis of $R_{bulk}$ values demonstrates that the incorporation of an HfO$_2$ overlayer significantly enhances charge transfer across the semiconductor-liquid junction (SCLJ) interface. This observation suggests that the HfO$_2$ overlayer plays a crucial role in suppressing surface recombination by effectively passivating surface defect states. It is also apparent that the modification of the Ba:BiVO$_4$/HfO$_2$ electrode with NiPt in particular at low applied bias potential further improves charge transfer. This improvement is expected as NiPt is confirmed to be a good catalyst for water oxidation and it can accelerate the hole transfer via the BiVO$_4$ valence band rather than SS. This behavior can be attributed to the strong electron exchange between Pt SA and Ni and the formation of covalent bonds between surface oxygen sites and NiPt atoms, which promotes charge transfer across the interface of Ba:BiVO$_4$/HfO$_2$ and NiPt with reduced bulk charge recombination.

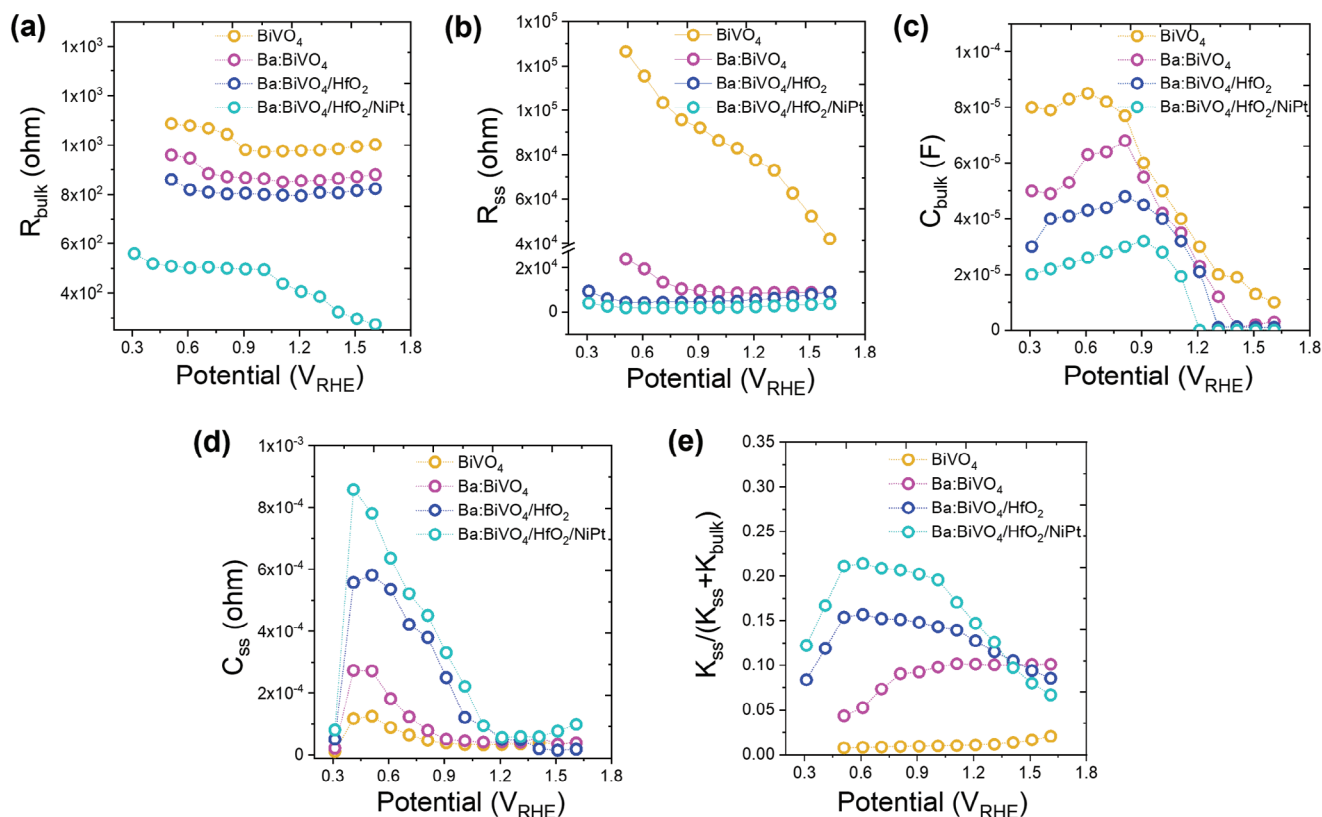**Figure 4.** Equivalent circuit parameters obtained from fitting EIS data for the $BiVO_4$, $Ba:BiVO_4$, $Ba:BiVO_4/HfO_2$, and $Ba:BiVO_4/HfO_2/NiPt$ electrodes under illumination. $R_{bulk}$ a), $R_{SS}$ b), $C_{bulk}$ c), $C_{SS}$ d), and $k_{SS}$ and $k_{bulk}$ ratios e) as a function of applied potential.

The surface trap resistance ($R_{SS}$), which relates to the charge transfer through SS to the electrolyte, follows the trend $BiVO_4 > Ba:BiVO_4 > Ba:BiVO_4/HfO_2 > Ba:BiVO_4/HfO_2/NiPt$ (Figure 4b). The $R_{SS}$ value is gradually decreased with increasing applied potential for the bare photoanode, whereas they leveled off in the range of 0.6–1.5 V for the $Ba:BiVO_4$, $Ba:BiVO_4/HfO_2$, and $Ba:BiVO_4/HfO_2/NiPt$ samples. The remarkable decrease in $R_{SS}$ demonstrates that Ba doping has a significant influence on the reduction of surface states.

Interestingly, the capacitance ($C_{bulk}$) associated with charge accumulation in the bulk shows a peak at 0.6–1.2 $V_{RHE}$ (Figure 4c). This behavior is attributable to charge accumulation due to the redox process of $V^{4+}/V^{5+}$ in the bulk. It is clear that the peak potential shifts to more positive values, whereas peak intensity decreases for $Ba:BiVO_4$, $Ba:BiVO_4/HfO_2$, and $Ba:BiVO_4/HfO_2/NiPt$ samples. This is consistent with the reduction peak of $V^{5+}$ to $V^{4+}$ in the same applied potential range. Moreover, the $C_{bulk}$ values for $Ba:BiVO_4/HfO_2/NiPt$ undergo a drop in potential, suggesting that the photogenerated holes accumulate at the semiconductor/co-catalyst interface until reaching a proper ratio between photogenerated holes and water-splitting oxidation intermediates. This supports the key role of the co-catalyst as a hole accumulation layer, which was also observed for other metal oxide/co-catalyst systems. The above results clearly demonstrate NiPt as a promising catalyst with a low onset potential and high photocurrent for PEC water oxidation. A similar discharge characteristic was also observed for all samples when considering the

surface state capacitance ($C_{SS}$), which arises from the accumulation of charges at SS (Figure 4e). Notably, the peaks observed for the $C_{SS}$ curves approximately coincided with the corresponding $V_{on}$ values for all samples.

Furthermore, a deeper investigation of the interfacial charge transfer process is required to highlight the role of the surface state. First, to ascertain the percentage of charge that is transferred for different electrodes, we estimate the charge proportion at the semiconductor/electrolyte interface through Equation (3):

$$K_{ss}/(K_{bulk} + K_{ss}) = 1/(1 + R_{ss}/R_{bulk}) \quad (3)$$

where $K_{bulk}$ and $K_{SS}$ are the rate constants for charge transfer in the bulk and SS, respectively. The charge transfer resistance is obtained from the fitting data of EIS, shown in Figure 4a–d. The resulting ratios as a function of the potential are shown in Figure 4e. A lower $R_{SS}$ and larger $R_{bulk}$ correspond to a larger proportion of charge transferred to water at the semiconductor/electrolyte interface. Therefore, $BiVO_4$ has fairly low values of charge transfer ratio across the applied potential range. This means that few charges are transferred to the electrolyte because they suffer from significant surface electron−hole recombination. In contrast, the surface recombination of photoanodes has been suppressed in $Ba:BiVO_4 < Ba:BiVO_4/HfO_2 < Ba:BiVO_4/HfO_2/NiPt$, respectively, leading to remarkable enhancement of charge transfer efficiency.

**ADVANCED
SCIENCE NEWS**

www.advancedsciencenews.com

**ADVANCED
ENERGY
MATERIALS**

www.advenergymat.de

## 2.4. Photoelectrochemical Stability

In addition to the high photocurrent efficiency, the high stability and durability of the photoelectrodes are also critical for practical applications. **Figure** 5a compares the current–time (*i–t*) curves of four types of photoanodes (pristine $BiVO_4$, $SnO_2/BiVO_4$, $SnO_2/Ba:BiVO_4$, and $SnO_2/BiVO_4/HfO_2$) operated at 1.23 $V_{RHE}$. Note that due to the serious photocorrosion and $V^{5+}$ dissolution from the crystal lattices, the pristine $BiVO_4$ exhibited a rapid decrease of the photocurrent, signifying a relatively poor PEC stability. Also, $BiVO_4$ can sometimes contain bismuth oxide phases on its surface due to oxidation or surface transformations. These phases can introduce additional energy levels within the bandgap, acting as recombination centers for charge carriers. This recombination reduces the lifetime of charge carriers and limits their ability to participate in efficient photocurrent generation. The $SnO_2$ (10 nm)/$BiVO_4$ photoanode film improves the stability up to 4 h, indicating that $SnO_2$ can block holes to suppress recombination via FTO-related defects at the FTO/$BiVO_4$ interface. It is worth noting that without the $SnO_2$ interfacial layer, the photoelectrons can be trapped at these defect sites, leading to accumulation of negative charges at the FTO/$BiVO_4$ interface. Additional electrons will be repelled by this negative charge and remain in the bulk. This reduces the band bending in $BiVO_4$ and allows the photogenerated holes to reach the FTO/$BiVO_4$ interface and recombine with the trapped electrons. This result reveals that $SnO_2$ plays an important role in stability by preventing the photogenerated holes from reaching the defect state. This leads to less recombination and a higher collection efficiency.[36]

Furthermore, $SnO_2/Ba:BiVO_4$ showed a significant photocurrent with 10 h stability, revealing that the substrate passivation and barium dopant increased the bulk charge separation (Figure 5a). We also verified the long-term stability of the $SnO_2/Ba:BiVO_4/HfO_2$ photoanode to understand the role of $HfO_2$ at the $BiVO_4$ interface. The photocurrent densities were fairly sustainable until 20 h, revealing excellent stability due to the conformal semi-crystalline $HfO_2$ protective layer. During the continuous illumination from 0–20 h, 95% of the initial photocurrent density was maintained for the photoanode with the $HfO_2$ overlayer, while there was as little as 25% photocurrent density left for the bare photoanode. To ensure reproducibility, these primary findings include $SnO_2$ underlayers, Ba ion dopants, and $HfO_2$ passivation tests performed repeatedly with different batch samples.

Finally, we deposited the single-atom NiPt co-catalysts on the $SnO_2/Ba:BiVO_4/HfO_2$ photoanode under similar conditions. The $Ba:BiVO_4/HfO_2/NiPt$ photoanode achieved good stability (≈800 h) while maintaining a high photocurrent density (≈6.5 mA cm$^{-2}$), presented in Figure 5b. These results clearly demonstrate that the decoration of NiPt catalysts not only significantly promotes the PEC activity but also effectively enhances the PEC stability of the $BiVO_4$ photoanodes. The surface morphology and composition of the photoanodes are almost unchanged after the 800-h stability test, demonstrating the promising role of $HfO_2$ and NiPt as protective layers against corrosion. To understand the surface morphology, we verified the structure and composition of the $SnO_2/Ba:BiVO_4/HfO_2/NiPt$ photoanode via HR-TEM analysis (Figure 5c–j) after the ≈800-h stability test. Importantly, no deformation of the morphology was observed, and

the $HfO_2$ passivation layer still protected the photoactive $BiVO_4$. The NiPt co-catalyst morphology was expanded like the bundle structure, implying that during the stability test, the composition reconstruction was unavoidable. This is likely due to the Ni-based catalyst in the form of hydroxide and oxy-hydroxide, which includes Pt active centers due to the re-deposition process. After long-term durability testing, the $Ni^0$ peak disappeared, while the $Ni(OH)_2$ peak gradually increased. The presence of $Ni^{3+}$ ions facilitate the generation of $Ni^{3+}(O)-OH$ intermediates. This is consistent with the XPS analysis of the sample after stability testing, presented in Figure S8a,b (Supporting Information). Meanwhile, the reconstruction process during PEC reaction can deduce to the formation of Pt@NiOOH or Pt@Ni(OH)$_2$ is more likely and can function as a robust OER catalyst. Moreover, the atomically dispersed NiPt catalyst was confirmed to be more stable against Pt dissolution. This attested that the atomically dispersed NiPt alloy was maintained after long stability testing and seen in Figure S9(a–c) (Supporting Information). The results indicate that Pt atoms are strongly anchored to the Ni, or $Ni(OH)_2$ or NiOOH lattice, preventing their migration and aggregation into larger clusters even under prolonged PEC conditions.

The rapid development of $BiVO_4$-based photoanodes has been achieved for enhanced photocurrent density and photostability, as summarized in Figure 5k.[17,18,28,37–40] According to state-of-the-art research, surface-engineered $BiVO_4$ photoanodes operate for ≈ 500 h under 1.23 $V_{RHE}$ and for ≈ 1100 h under 0.4 $V_{RHE}$. A noteworthy feature of our photoanode film is that it achieved high photocurrent density and operated for up to ≈800 h with minimal photocurrent loss, even at 1.23 $V_{RHE}$. During steady-state testing, the photoanode was more stable due to the lattice stabilization by isolated NiPt atoms with high active site energy as well as the formation of the Ni-O-Pt bond without obvious dissolution or clustering during the durability test.

## 3. Conclusion

In summary, we demonstrated a Ba-doped $BiVO_4$ electrode composed of $HfO_2$ (≈10 nm) passivation with a NiPt co-catalyst for the PEC water oxidation under mild alkaline conditions. The $HfO_2$ passivated photoanode exhibits a cathodic onset shift (0.28 $V_{RHE}$) with a large current density, which can be attributed to surface defect passivation by $HfO_2$ facilitating an efficient charge transfer event. In particular, $Ba:BiVO_4$-induced excessive oxygen vacancies can act as active intermediates for the water oxidation reaction in the presence of $V^{4+}$ species. Detailed electrochemical analysis using EIS revealed the charge transfer/recombination processes of $Ba:BiVO_4/HfO_2/NiPt$. The synergistic interaction between isolated single-atom sites and Ni—Pt coordination within the $Ba:BiVO_4/HfO_2/NiPt$ architecture results in exceptional charge transfer and separation at the photoanode surface, significantly enhancing PEC performance and operational stability. This remarkable design achieved a record durability exceeding 800 h, exhibiting negligible degradation at ≈6.5 mA cm$^{-2}$ at 1.23 V versus RHE under AM 1.5 illumination. This study will pave a new path for addressing the challenge of durable, long-term photoelectrode operation for energy conversion applications.
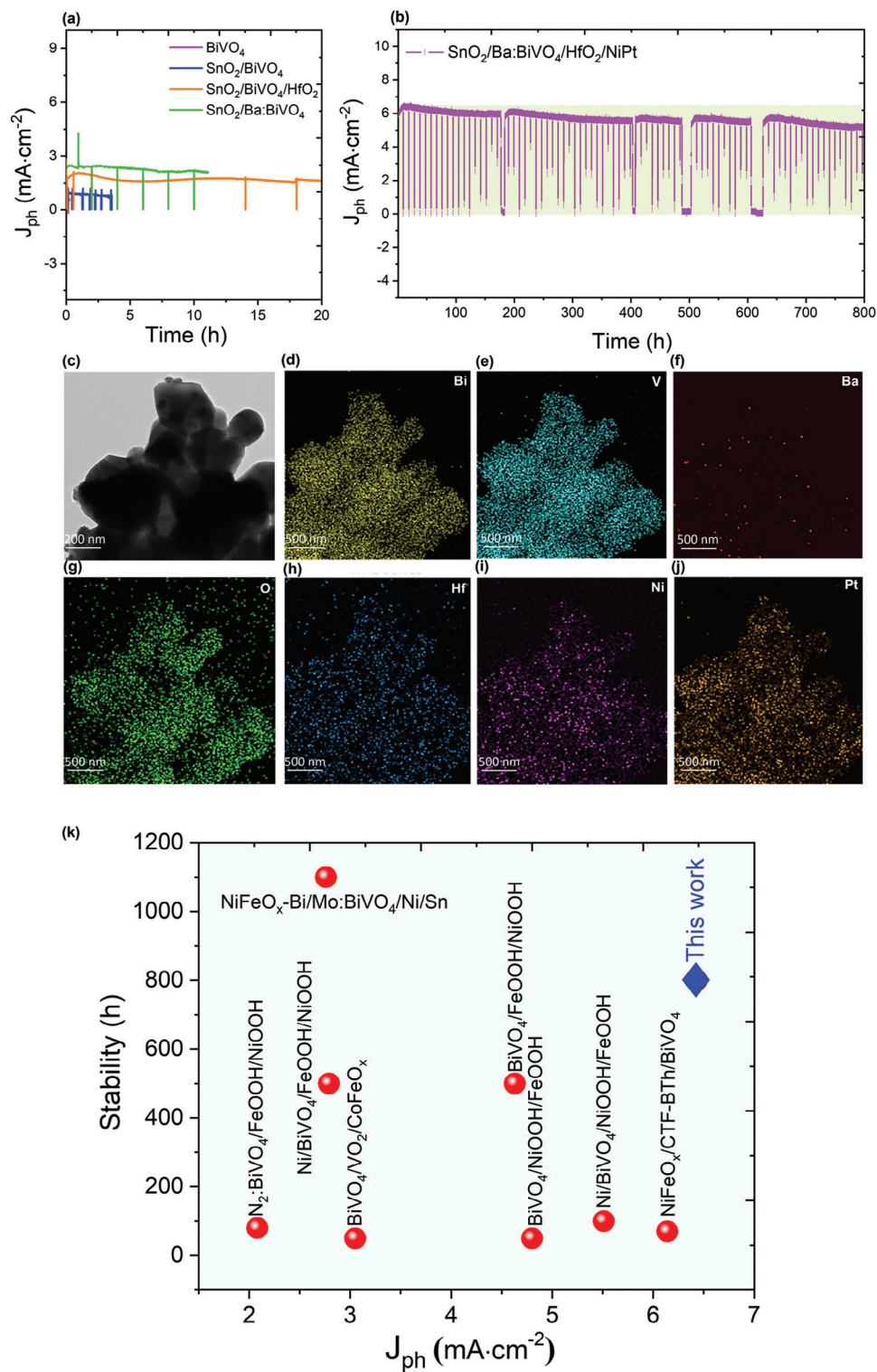
**Figure 5.** a) and b) Stability test of the photoanode films (at 1.23 $V_{RHE}$), c) HR-TEM image of $BiVO_4/HfO_2/NiPt$ after 800-h stability test, d–j) EDS mapping of elements such as Bi, V, Ba, Hf, O, Ni, and Pt after 800-h stability test, and k) the photocurrent density and stability of recent reported $BiVO_4$ photoanode films.

## 4. Experimental Section

*Materials*: Sulfuric acid ($H_2SO_4$, 98%, DAEJUNG), Hydrogen peroxide ($H_2O_2$, 28%, DUKSAN), Anhydrous ethanol ($C_2H_5OH$, DAEJUNG), Acetone ($C_3H_6O$, DAEJUNG), Bismuth (III) nitrate pentahydrate ($Bi(NO_3)_3 \cdot 5H_2O$, Sigma-Aldrich, 98%), Vanadium(V) oxytripropoxide ($C_9H_{21}O_4V$, 99+%, Alfa Aesar), Barium nitrate ($Ba(NO_3)_2$, Dimethylformamide (DMF anhydrous, 99.8%, Sigma-Aldrich), Dimethyl sulfoxide (($CH_3)_2SO$, 99+%, Alfa Aesar), Sodium hydroxide (NaOH, flake (98%), Chloroplatinic acid hexahydrate ($H_2PtCl_6 \cdot 6H_2O$, 99.9%, Sigma-Aldrich), Nickel(II) chloride hexahydrate ($NiCl_2.6H_2O$, DC chemical), Boric acid ($H_3BO_3$, 99.5%, OCI), high pure nitrogen ($N_2$, 99.999%, Shinbiochem), the deionized (DI) water, with a resistivity of 18.25 MΩ cm$^{-1}$, used in all experiments were prepared using ultrapure purification systems (PURELAB, Elgalab).

*Fabrication of the Ba-Doped BiVO$_4$ Photoanode Film*: FTO glass substrates (58–72 ohm sq.$^{-1}$, MTIKOREA) were ultrasonically cleaned in acetone, DI water, and ethanol for 15 min each, followed by a chemical etching treatment in a 1:1:3 ratio of $H_2O$:$H_2O_2$:$H_2SO_4$ for 15 min. This procedure promotes strong film adhesion and ensures uniform deposition of the photoanode. The 10 nm thick $SnO_2$ layer was deposited onto the cleaned FTO using atomic layer deposition (ALD, NCD (Lucida D100)) employing tetrakis(dimethylamino)tin(IV) (TDMASn, 99.99% Sn, Strem Chemicals) and water as precursors. A consistent growth rate of 0.014 nm per cycle was verified by alpha-step measurements, and nitrogen (99.9999%) was used as the carrier gas at a flow rate of 50 sccm. The Sn sub-cycle consisted of the following steps: 2 s of TDMASn pulse, followed by 15 s of $N_2$ purge, then 2 s of $H_2O$ pulse, and finally 15 s of $N_2$ purge. The as-deposited films were then annealed in a muffle furnace at 400 °C for 30 min. For Bi electrodeposition, 0.04 м $Bi(NO_3)_3 \cdot 5H_2O$ was dissolved in 25 mL DMF and 25 mL DI water. The above solution was purged with Ar gas for 30 min. A constant potential of −1.5 V$_{Ag/AgCl}$ was applied for 3 min to fabricate the $BiVO_4$ photoanode film. Then, $C_9H_{21}O_4V$ in DMSO was placed on the as-prepared film and dried at 50 °C in an oven for 10 min before annealing at 450 °C for 2 h in air. Excess $V_2O_5$ was removed by dipping in an alkali solution and the film was rinsed with DI water and dried in nitrogen. For barium doping, the electrochemical bath solution was prepared with the appropriate amount of $Ba(NO_3)_2$, while all other processes remained the same as for the pristine $BiVO_4$.

*Fabrication of HfO$_2$ Passivation Layer over Ba-Doped BiVO$_4$ Photoanode Film*: ALD of $HfO_2$ was performed at 150 °C using a Lucida D100 system from NCD. Tetrakis(ethylmethylamino)hafnium (TEMAH) served as the hafnium precursor, and DI water was used as the oxygen source. The temperature of the hafnium precursor was kept at 40 °C, while DI water was kept at room temperature. High-purity $N_2$ (99.9999%) was the carrier and purging gas. Under these deposition conditions, one ALD growth cycle consisted of the following sequence: tetrakis(ethylmethylamino)hafnium pulse, followed by an $N_2$ purge, then an $H_2O$ pulse, and a final $N_2$ purge. The Ba:BiVO$_4$ photoanode was coated with $HfO_2$ using different ALD cycle numbers: 50, 75, and 100, resulting in film thicknesses of 5, 10, and 15 nm, respectively. The thickness was determined from a growth rate of 0.14 nm per ALD cycle, using ellipsometry measurements with a Veeco Dektak 150 ellipsometer.

*Deposition of NiPt over Ba:BiVO$_4$/HfO$_2$ Photoanode*: For NiPt deposition, 0.2 м $NiCl_2.6H_2O$, 0.2 м $H_3BO_3$, and 3 mM $H_2PtCl_6 \cdot 6H_2O$ were dissolved in 50 mL of DI water, and 1 mL of 0.5 м KCl was then added to the solution. Electrochemical deposition was performed in a three-electrode cell comprising the Ba:BiVO$_4$/HfO$_2$ photoanode as the working electrode, Pt foil as the counter electrode, and saturated Ag/AgCl as the reference electrode. A constant potential of −0.8 V was applied for 100 s. The as-deposited NiPt composite was then cleaned with ethanol and DI water and dried in $N_2$ gas. The fabricated samples were designated as Ba:BiVO$_4$/HfO$_2$/NiPt.

## Supporting Information

Supporting Information is available from the Wiley Online Library or from the author.

## Conflict of Interest

The authors declare no conflict of interest.

## Data Availability Statement

The data that support the findings of this study are available from the corresponding author upon reasonable request.

[1] J. H. Kim, D. Hansora, P. Sharma, J. W. Jang, J. S. Lee, *Chem. Soc. Rev.* **2019**, *48*, 1908.

[2] B. A. Pinaud, J. D. Benck, L. C. Seitz, A. J. Forman, Z. Chen, T. G. Deutsch, T. F. Jaramillo, *Energy Environ. Sci.* **2013**, *6*, 1983.

[3] S. Wang, P. Chen, J. H. Yun, Y. Hu, L. Wang, *Angew. Chem., Int. Ed.* **2017**, *56*, 8500.

[4] C. Jiang, S. J. Moniz, A. Wang, T. Zhang, J. Tang, *Chem. Soc. Rev.* **2017**, *46*, 4645.

[5] T. W. Kim, K. S. Choi, *Science* **2014**, *343*, 990.

[6] H. S. Han, S. Shin, D. H. Kim, I. J. Park, J. S. Kim, P. S. Huang, X. Zheng, *Energy Environ. Sci.* **2018**, *11*, 1299.

[7] J. Jian, Y. Xu, X. Yang, W. Liu, M. Fu, H. Yu, H. Wang, *Nat. Commun.* **2019**, *10*, 2609.

[8] J. K. Cooper, S. Gul, F. M. Toma, L. Chen, P. A. Glans, J. Guo, I. D. Sharp, *Chem. Mater.* **2014**, *26*, 5365.

[9] F. F. Abdi, L. Han, A. H. Smets, M. Zeman, B. Dam, R. Van De Krol, *Nat. Commun.* **2023**, *4*, 2195.

[10] Y. J. Jeong, D. H. Seo, J. H. Baek, M. J. Kang, B. N. Kim, S. K. Kim, I. S. Cho, *Adv. Funct. Mater.* **2022**, *32*, 2208196.

[11] Q. Shi, S. Murcia-López, P. Tang, C. Flox, J. R. Morante, Z. Bian, T. Andreu, *ACS Catal.* **2018**, *8*, 3331.

[12] W. J. Jo, J. W. Jang, K. J. Kong, H. J. Kang, J. Y. Kim, H. Jun, J. S. Lee, *Angew. Chem., Int. Ed.* **2012**, *51*, 3147.

**ADVANCED
SCIENCE NEWS**

www.advancedsciencenews.com

**ADVANCED
ENERGY
MATERIALS**

www.advenergymat.de

[13] R. T. Gao, D. He, L. Wu, K. Hu, X. Liu, Y. Su, L. Wang, *Angew. Chem.* **2020**, *132*, 6272.

[14] B. Zhang, L. Wang, Y. Zhang, Y. Ding, Y. Bi, *Angew. Chem., Int. Ed.* **2018**, *57*, 2248.

[15] E. Usman, M. Barzgar Vishlaghi, A. Kahraman, N. Solati, S. Kaya, *ACS Appl. Mater. Interfaces* **2021**, *13*, 60602.

[16] S. Zhang, Z. Liu, D. Chen, W. Yan, *Appl. Catal., B* **2020**, *277*, 119197.

[17] Y. Kuang, Q. Jia, G. Ma, T. Hisatomi, T. Minegishi, H. Nishiyama, K. Domen, *Nat. Energy* **2016**, *2*, 16191.

[18] T. W. Kim, Y. Ping, G. A. Galli, K. S. Choi, *Nat. Commun.* **2015**, *6*, 8769.

[19] J. Zhang, Y. Yuan, L. Gao, G. Zeng, M. Li, H. Huang, *Adv. Mater.* **2021**, *33*, 2006494.

[20] K. Shah, R. Dai, M. Mateen, Z. Hassan, Z. Zhuang, C. Liu, Y. Li, *Angew. Chem.* **2022**, *134*, 202114951.

[21] F. Jiang, Y. Li, Y. Pan, *Adv. Mater.* **2024**, *36*, 2306309.

[22] C. Balamurugan, Y. Y. Kim, Y. R. Jo, K. Cho, B. Park, W. Kim, W. S. Kwon, *Appl. Catal., B* **2024**, *353*, 124072.

[23] H. Jin, P. Li, P. Cui, J. Shi, W. Zhou, X. Yu, C. Cao, *Nat. Commun.* **2022**, *13*, 723.

[24] L. Huo, C. Jin, J. Tang, X. Xu, K. Jiang, L. Shang, Z. Hu, *ACS Appl. Energy Mater.* **2022**, *5*, 15136.

[25] M. Arunachalam, Y. J. Seo, S. Jeon, K. S. Ahn, C. S. Kim, S. H. Kang, *Chem. Eng. J.* **2020**, *394*, 125016.

[26] Y. Zhang, L. Xu, B. Liu, X. Wang, T. Wang, X. Xiao, W. Huang, *ACS Catal.* **2023**, *13*, 5938.

[27] Z. Tian, P. Zhang, P. Qin, D. Sun, S. Zhang, X. Guo, F. Huang, *Adv. Energy Mater.* **2019**, *9*, 1901287.

[28] R. T. Gao, S. Liu, X. Guo, R. Zhang, J. He, X. Liu, L. Wang, *Adv. Energy Mater.* **2021**, *11*, 2102384.

[29] J. B. Pan, B. H. Wang, J. B. Wang, H. Z. Ding, W. Zhou, X. Liu, S. F. Yin, *Angew. Chem.* **2021**, *60*, 1433.

[30] B. Liu, X. Wang, Y. Zhang, L. Xu, T. Wang, X. Xiao, W. Huang, *Angew. Chem.* **2023**, *135*, 202217346.

[31] H. Pei, L. Peng, Z. Jiang, Y. Zhang, R. Li, T. Peng, *Adv. Funct. Mater.* **2024**, *34*, 2401122.

[32] C. Zhou, L. Ma, Y. Feng, C. Y. Kuo, Y. C. Ku, C. E. Liu, Z. Chen, *Nat. Commun.* **2024**, *15*, 2893.

[33] C. Balamurugan, C. Lee, K. Cho, J. Kim, B. Park, W. Kim, S. Kwon, *Appl. Catal., B* **2023**, *330*, 122631.

[34] D. Li, Y. Liu, W. Shi, C. Shao, S. Wang, C. Ding, C. Li, *ACS Energy Lett.* **2019**, *4*, 825.

[35] A. R. Bredar, A. L. Chown, A. R. Burton, B. H. Farnum, *ACS Appl. Energy Mater.* **2020**, *3*, 66.

[36] S. Bera, S. A. Lee, W. J. Lee, J. H. Kim, C. Kim, H. G. Kim, S. H. Kwon, *ACS Appl. Mater. Interfaces* **2021**, *13*, 14291.

[37] D. S. Kim, K. W. Lee, J. H. Choi, H. H. Lee, H. W. Suh, H. S. Lee, H. K. Cho, *J. Mater. Chem. A* **2022**, *10*, 21300.

[38] S. Wang, P. Chen, Y. J. H. Yun, G. Liu, L. Wang, *Adv. Mater.* **2018**, *30*, 1800486.

[39] Y. Zhang, H. Lv, Z. Zhang, L. Wang, X. Wu, H. Xu, *Adv. Mater.* **2021**, *33*, 2008264.

[40] R. T. Gao, L. Wu, S. Liu, K. Hu, X. Liu, J. Zhang, L. Wang, *J. Mater. Chem. A* **2021**, *9*, 6298.